Appl Phys B (2011) 105:113–127
DOI 10.1007/s00340-011-4681-2

Applied Physics B
Lasers and Optics

Structuring of material parameters in lithium niobate crystals with low-mass, high-energy ion radiation

K. Peithmann · P.-D. Eversheim · J. Goetze · M. Haaks · H. Hattermann · S. Haubrich · F. Hinterberger · L. Jentjens · W. Mader · N.L. Raeth · H. Schmid · M.-R. Zamani-Meymian · K. Maier

Received: 30 March 2011 / Revised version: 13 May 2011 / Published online: 31 August 2011

Abstract Ferroelectric lithium niobate crystals offer a great potential for applications in modern optics. To provide powerful optical components, tailoring of key material parameters, especially of the refractive index n and the ferroelectric domain landscape, is required. Irradiation of lithium niobate crystals with accelerated ions causes strong structured modifications in the material. The effects induced by low-mass, high-energy ions (such as ^{3}He with 41 MeV, which are not implanted, but transmit through the entire crystal volume) are reviewed. Irradiation yields large changes of the refractive index Δn, improved domain engineering capability within the material along the ion track, and waveguiding structures. The periodic modification of Δn as well as the formation of periodically poled lithium niobate (PPLN) (supported by radiation damage) is described. Two-step knock-on displacement processes, $^3\text{He}\rightarrow\text{Nb}$ and $^3\text{He}\rightarrow\text{O}$ causing thermal spikes, are identified as origin for the material modifications.

1 Introduction

Lithium niobate crystals ($LiNbO_3$) draw much attention due to their potential in technological applications. They offer superior optical properties making them very interesting for many applications, owing to their mechanical stability and optical homogeneity. Great efforts have been undertaken in engineering holographic memories [1–4], based on the photorefractive effect [5, 6], and holographic filters for telecommunication purposes [7, 8]. Lithium niobate crystals can also serve as base material for components used in integrated optics, such as couplers [9] and modulators [10, 11] with waveguiding structures [12, 13]. Integrated lasers [14] using thermally fixed photorefractive refractive-index gratings [15, 16] are another interesting employment. Doping of the crystals is also possible either by adding suitable dopants to the melt during the crystal growth process, or by diffusion techniques applied to pure crystalline material [17, 18]. All these applications require large, stable, and well-designed changes of the refractive index Δn or, to be more exact, of the two refractive indices, the ordinary Δn_o and the extraordinary Δn_e. The ferroelectric $LiNbO_3$ crystals are optically uniaxial, having a polar c axis. Detailed knowledge about the effect of ion irradiation on other important material parameters, such as the ferroelectric coercive field E_C or the electrical conductivity, σ, is required, too.

In this review, several aspects regarding structured material modifications in $LiNbO_3$ crystals upon the irradiation with high-energy ions are covered. Section 2 will focus on changes of the refractive index Δn caused by the ions. Furthermore, structured modifications of the ferroelectric domains of $LiNbO_3$ are desired: Sect. 3 will show how ion exposure can be used to assist the formation of small-sized domain patterns. Section 4 will deal with changes of the electrical conductivity upon ion exposure, and in Sect. 5 we look at the ion-induced material changes on a microscopic scale by using transmission electron microscopy (TEM). Section 6 will summarize the insights gained before and discuss the microscopic processes. Finally, in Sect. 7 the formation of an embedded waveguide as an application will be shown.

K. Peithmann (✉) · P.-D. Eversheim · J. Goetze · M. Haaks · H. Hattermann · S. Haubrich · F. Hinterberger · L. Jentjens · N.L. Raeth · M.-R. Zamani-Meymian · K. Maier
Helmholtz-Institut für Strahlen- und Kernphysik, Universität Bonn, Nussallee 14–16, 53115 Bonn, Germany
e-mail: peithman@physik.uni-bonn.de

W. Mader · H. Schmid
Institut für Anorganische Chemie, Universität Bonn, Römerstr. 164, 53115 Bonn, Germany

2 Changes in refractive index

Changing the refractive index of $LiNbO_3$ has been performed by irradiation of the crystals with ions. This technique is preferentially used in order to form waveguides in the material by ion implantation [13, 19, 20]. Here ions such as ^{4}He with an energy of some MeV are used. The ions have a range within the crystals of about 50 μm before they are stopped within a thin layer (so-called Bragg peak). A major fraction of the ion energy is dissipated within this thin Bragg peak, yielding extensive material damage and large parameter changes. In particular, significant modifications of the refractive index are present within this thin layer, forming an index barrier between the substrate and the material which has been penetrated by the ions. If the refractive-index change in the Bragg peak is negative, light can be guided in the crystal slab between the surface and the Bragg layer. However, the optical properties of the crystal volume which has been subjected to ion penetration is of special interest, too, because the light will be guided here. In an initial approach, this layer has been assumed to be almost unchanged. More detailed investigations of the waveguides produced by the ion-implantation technique showed that the ordinary index n_o is slightly reduced and the extraordinary index n_e is enhanced in the light-guiding region [21–23], but these changes have not been directly determined. Furthermore, an increase of n_e within the Bragg layer has been reported [24], controversial to the other literature reports mentioned before. Hence, if well-designed changes of the refractive index n are desired, more detailed knowledge about their formation processes is necessary.

A slightly modified method of ion implantation should be mentioned: if larger ions (so-called swift heavy ions, such as Si, F, Cu, N, or O) are utilized, strong modifications of the crystals can be achieved, even if substantially lower ion fluences are used, compared to low-mass ions [25–27]. The electronic energy loss of these ions is supposed to be large enough to cause very impressive material damage; even an amorphization of crystal layers is reported, attributed to the part of the ion track where the energy loss $\Delta E/\Delta x$ has its largest value [28]. Since the refractive index in the amorphous layer ($n = 2.1$ at $\lambda = 633$ nm) is much lower than both the ordinary index ($n_\mathrm{o} = 2.28$ at 633 nm) as well as the extraordinary index ($n_\mathrm{e} = 2.20$ at 633 nm) [29], light can be guided between this amorphous layer and the surface, thus enabling the formation of highly confined waveguides. However, the optical properties of the light-guiding material are changed by the transmitted ions, too, and so far we have very limited knowledge about the processes responsible for these changes.

Using ions with very high energies (up to 16 MeV/nucleon) can extend the crystal layer which is transmitted through by the ions (without getting them implanted) by shifting the Bragg peak to deep crystal regions. If low-mass ions (such as alpha particles or ^{3}He) with energies of some 10 MeV/nucleon are used, the Bragg peak lies at a depth of some hundreds of micrometers. Hence, using crystals thinner than this range will allow us to investigate the material properties in the region of pure transmission (and not ion implantation). Very large changes of the refractive index of up to 6×10^{-3} have been reported if $LiNbO_3$ crystals are subjected to ion penetration with alpha particles or deuterons [30]. Detailed investigations of these changes Δn inside the transmitted crystal volume between the surface and the Bragg peak upon ion exposure with low-mass, high-energy ions will be summarized within the next paragraphs. Furthermore, methods for the periodic structuring of the refractive index of $LiNbO_3$ will be targeted.

2.1 Irradiation treatments with low-mass, high-energy ions

The irradiations are carried out at the cyclotron of the Helmholtz-Institut für Strahlen- und Kernphysik, Universität Bonn. We use doubly ionized ^{3}He ions which are accelerated to an energy of 41 MeV. Ions with this energy have a quite long range within $LiNbO_3$ crystals: calculations using the software tool SRIM-2006 [31] yield a range of 0.53 mm. Since the ion range exceeds the typical crystal thickness of 0.5 mm, at least 99.9% of the ^{3}He ions are transmitted through the entire crystal; the ions are not implanted into the material. Choosing ^{3}He ions offers a good compromise between radiation effects caused by the ions and parasitic nuclear activation of the target material: the activation rate is quite low, and the radioactive nuclei created have short decay times. The irradiated crystals lose their activity typically within a few weeks. However, similar radiation effects can be achieved using ^{4}He (alpha particles) or deuterons [30]. During the irradiation, the crystals are mounted on an aluminum heat sink using a heat-conductive paste [32]; the setup is mounted in a vacuum recipient. Alternatively, the crystals are placed behind a thin aluminum foil (thickness $t = 100$ μm) to be separated from the cyclotron vacuum [33]: here thermal protection of the samples is achieved by spilling cooling water around the crystal. The dimensions of the ion beam are varying between a circular shape (diameter ≈5 mm with a Gaussian-shaped intensity distribution) and a slit-like spot with dimensions of 2×7 mm^2. The total ion current can be tuned up to 1 μA at an irradiation duration ranging from minutes up to 6 h. This corresponds to a peak ion fluence of up to 1.6×10^{21} m^{-2}.

We use commercially available $LiNbO_3$ crystals purchased from Yamaju Ceramics, Japan. Our samples are cut from wafer material to pieces with typical dimensions of $(x \times y \times z) = (0.5 \times 9 \times 10)$ mm^3 (x-cut samples) or

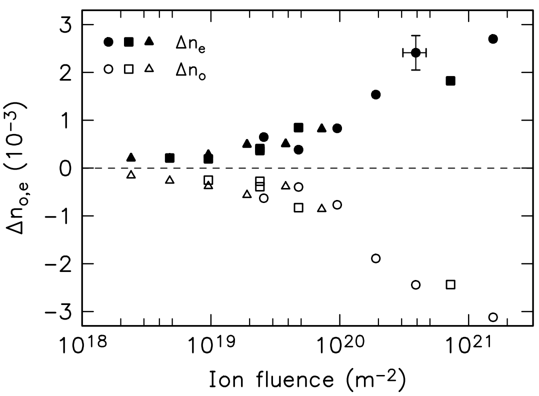

Fig. 1 Refractive-index changes for ordinary (Δn_o) and extraordinary (Δn_e) light polarizations versus total ion fluence measured in undoped, congruently melting LiNbO$_3$. The different symbols represent data for three different sets of measurements [33]

$(x \times y \times z) = (16 \times 15 \times 0.5)\ \text{mm}^3$ (z-cut samples), where the crystallographic c axis is parallel to the z direction. The crystals are congruently melting, and we utilize either undoped material or magnesium-doped crystals with a Mg content of 5 mol%, exceeding the so-called threshold regarding optical damage resistivity.

2.2 Macroscopic refractive-index changes

Structural modifications inflicted by the high-energy ions on their trajectory through the crystal result in a change of the refractive index Δn [30]. Because the changes are quite stable and the absolute values are impressively large, these processes are studied in more detail. Changes in the refractive index are measured by interferometric techniques [34, 35] for both the ordinary Δn_o and extraordinary Δn_e refractive indices at the probe wavelength $\lambda = 633$ nm.

2.2.1 Dependences on dose and depth

Increasing the total ion fluence from 10^{18} up to $10^{21}\ \text{m}^{-2}$, the overall change of the refractive index increases significantly, as shown in Fig. 1 for three different data sets. The extraordinary index n_e grows, whereas the ordinary index n_o is diminished. The absolute values of Δn_e and Δn_o are comparable. Thus, the birefringence of the crystal gets smaller with increasing ion fluence. Large absolute values of Δn of up to 3×10^{-3} are achieved; even larger values are possible because saturation is not yet reached. However, even at low doses there are already quite remarkable changes, e.g. $\Delta n = 5 \times 10^{-4}$ at an ion fluence of $5 \times 10^{19}\ \text{m}^{-2}$ [33]. Changes of the refractive index measured in magnesium-doped crystals are similar to those observed in undoped material [32].

The total refractive-index changes as shown so far represent averaged values, because they are measured in a geometry with the probe light parallel to the direction of ion irradiation. A more detailed view is offered when we investigate the changes Δn as a function of the ion depth d along their track through the material. For this purpose, a small crystal stick with dimensions of $(x \times y \times z) = 1 \times 1 \times 6\ \text{mm}^3$ is used which is irradiated from the yz side. The subsequent interferometric measurement takes place through the xz surface. Two regions of interest are chosen: one is located in the center of the ion-beam spot where the ion intensity is large (position A), and the second focuses on a crystal part where a very low ion intensity is present (position B). The results are shown in Fig. 2 for both light polarizations (solid lines).

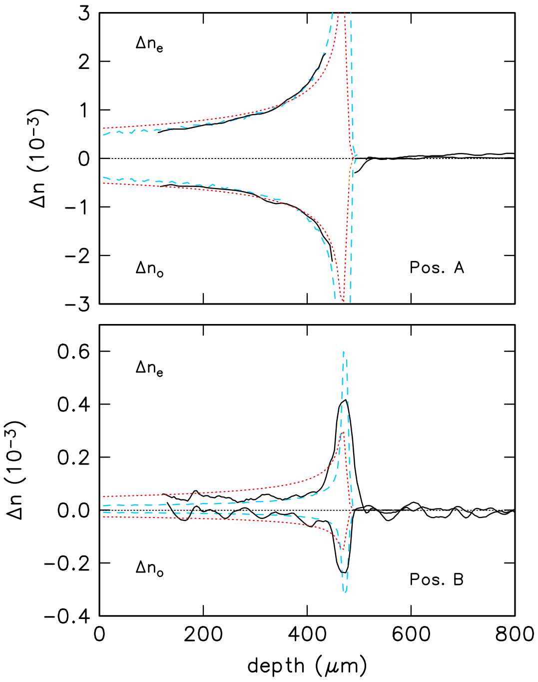

Fig. 2 Refractive-index changes for ordinary (Δn_o) and extraordinary (Δn_e) light polarizations vs crystal depth d at two different positions (A) in the maximum of the ion beam with large ion fluence (and hence large refractive-index changes) and (B) at the edge of the beam at a small ion fluence where the stop depth can be resolved. Experimental data are represented by the *solid lines*. The *dashed lines* (*blue*) show the density of vacancies per ion and angstrom $c_{\text{vac}}(d)$ as calculated using SRIM-2006, fitted by an arbitrary factor; *dotted lines* (*red*) indicate the particle energy loss per angstrom $\Delta E/\Delta x(d)$ [33]

A significant increase of the changes $\Delta n_{o,e}$ along the ion penetration depth d (and thus decreasing ion energy) is observed up to the Bragg peak. The ions are stopped at a depth of ≈0.47 mm in the water-cooled setup with an Al foil placed in front of the crystal (thickness $t = 100$ μm), causing an attenuation of the ion energy [31, 33]. Due to very large effects close to the Bragg peak, our interferometer cannot resolve Δn in the vicinity of the stop depth in region A. A similar problem occurs close to the surface, where no reliable measurement is possible. However, in region B even the Bragg peak can be evaluated: an increase of n_e as well as a decrease of n_o is present, even in the region of maximum radiation damage. Using SRIM-2006, the density of lattice vacancies per ion and angstrom $c_{vac}(d)$ is calculated. The curve $c_{vac}(d)$ shows qualitatively the same behavior as $\Delta n_{o,e}(d)$. In Fig. 2, $c_{vac}(d)$ is plotted as dashed lines, multiplied by an arbitrary factor. Obviously, the density $c_{vac}(d)$ corresponds to $\Delta n_{o,e}$. Another correlation could be assumed between $\Delta n_{o,e}(d)$ and the ion energy loss $\Delta E/\Delta x(d)$ per ion and angstrom. The curve $\Delta E/\Delta x(d)$ has a similar form with a maximum at the Bragg peak. This is also illustrated in Fig. 2, where $\Delta E/\Delta x(d)$, multiplied by an arbitrary factor, is plotted as dotted lines. It becomes obvious that the profiles $\Delta n_{o,e}(d)$ are distinctly better described by the density of vacancies $c_{vac}(d)$ than by the energy loss $\Delta E/\Delta x(d)$. This correlation is most obvious in regions close to the surface and within the vicinity of the Bragg peak.

2.2.2 *Thermal and long-term stability*

The changes $\Delta n_{o,e}$ are long-term stable, and they are robust against thermal treatments. This has been discovered for ion-implanted waveguides [22] as well as for the changes in the transmitted crystal volume [33]. At a temperature of 200°C, it requires 70 days to diminish $\Delta n_{o,e}$ down to 50% of its initial value [36]. To remove Δn completely, a heat treatment at 400°C for one week is necessary. The temporal behavior of the decay $\Delta n_{o,e}(t)$ vs time cannot be described by simple mono-exponential laws; at least three exponential components are needed [36]. When keeping a sample at room temperature, however, no decay can be observed within at least 4 years [36].

Comparing the temporal evolution of Δn to those exhibited by refractive-index changes fabricated by short-pulse (fs) laser writing, striking differences are obvious: other than the ion-fabricated changes, the fs-laser-induced Δn_e can be completely removed by moderate annealing [37]. Furthermore, the absolute values of Δn_e and Δn_o are different in the case of short-pulse-written changes, whereas the values are almost equal in the case of ion-radiation-based changes. This implies clear differences in the underlying microscopic mechanisms.

2.2.3 *Asymmetry as function of irradiation direction*

So far, we have neglected any dependence of Δn on the direction of the ion exposure with respect to the crystallographic axes. Using z-cut samples, two possible configurations can be chosen: the irradiation parallel (⇉) or antiparallel (⇄) to the c axis. Six crystals are irradiated consecutively with similar ion-beam parameters; those six crystals form three pairs, each consisting of one ⇉ and one ⇄ sample. After the irradiation, the changes Δn_o are evaluated.

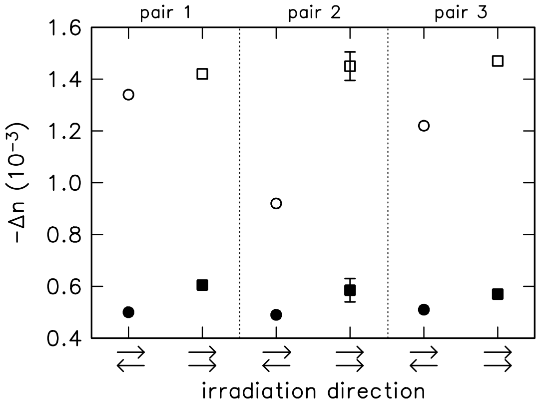

Fig. 3 Refractive-index changes Δn_o for six crystals arranged in three crystal pairs. The open symbols represent the maximum value for Δn_o^{max}, whereas the filled symbols show the results for an averaged Δn_o^{av} over the entire irradiated area. The circles indicate ion exposures performed with the ion direction antiparallel to the c axis (⇄), whereas the squares show data for parallel irradiation geometry (⇉) [38]

Due to the z-cut crystal geometry, we have access to the ordinary index only. Because the peak value for Δn_o depends very sensitively on the ion-beam profile, we apply a second evaluation technique to our data: we calculate an averaged value Δn_o^{av} over the entire irradiated area. This accounts for the sum of all changes caused by the ion exposure and yields a more reliable metric for the total effect caused by a certain ion fluence. The results for the three pairs of crystals are shown in Fig. 3: the open symbols represent the measured maximum values Δn_o^{max}, whereas the filled symbols stand for the averaged ones. Furthermore, the circles show data for the ⇄ configuration, and the squares indicate results for the ⇉ configuration.

Two results have to be emphasized: (1) the results are reproducible; within the experimental error, the numbers for the peak values as well as for the averaged values are equal. An exception is the ⇄ maximum result for pair 2. Here the ion beam was unstable, leading to a reduced maximum at identical total ion fluence and hence comparable averaged value for Δn_o^{av}. (2) The value for the ⇄ configuration is always distinctly smaller than for ⇉ irradiations. A clear asymmetry depending on the irradiation direction with respect to the crystal axis is observed. We will find a similar effect in the electrical conductivity σ (see below) and will discuss the reason for this asymmetry later in Sect. 4.

2.3 Color changes upon ion exposure

Radiation damage upon irradiation of $LiNbO_3$ with ions is accompanied by a characteristic change of the crystal color: the initially transparent material becomes brown in the ion-treated area. In particular, a broad absorption band centered at 500 nm appears [30, 39, 40]. The latter two references refer to irradiation of $LiNbO_3$ with electrons, yielding an absorption band similar to that induced by thermal reduction treatments. The absorption band upon irradiation with fast ions is slightly different, as described in Ref. [30], but it is reasonable to assume that these differences are revealed by better spectroscopy techniques. The brown color is a very good indicator of whether the crystal has been subjected to ion exposure and hence ion treatments have been successful. However, the absorption band is not as stable as the refractive-index changes: the color vanishes within a few weeks at room temperature, and it can also be removed by moderate annealing (for example at 100°C for 30 min) [30]. Hence, it can be attributed to changes in the electronic structure of the crystals (such as the formation of bipolarons in the vicinity of antisite defects [41] or the creation of color centers). Alternatively, ion vacancies within the oxygen lattice [39] can be considered. The latter however may be less reasonable in the case of ion-exposed $LiNbO_3$ because the color disappears at room temperature; hence, a rather low thermal activation energy is needed to anneal the damage causing the absorption.

2.4 Refractive-index gratings

As shown above, the changes Δn are quite stable. Hence, the formation of refractive-index gratings using radiation damage is a very interesting perspective. We will discuss three different approaches to craft gratings in $LiNbO_3$.

2.4.1 *Al–Ta foil stack*

Creating a grating in $LiNbO_3$ requires a grating-like ion-exposure pattern. One way to provide this is a suitable filter which consists of absorbing and permeable stripes. This concept is illustrated in Fig. 4. Tantalum stripes with a width (with respect to the direction of the ions) of 0.3 mm absorb the ions completely. Aluminum stripes allow the ions to travel through the filter with a certain energy loss; however, the ion energy remaining after transmitting 0.3-mm aluminum is still sufficient to reach a stop depth of 0.3 mm in $LiNbO_3$, as deduced from SRIM simulations [31]. We construct such a filter using tantalum and aluminum foils with a thickness of 3 μm which are cut into small stripes of 1×5 mm^2. These foils are stacked 100 times. To enclose them, a tantalum mount with a slot is mechanically milled. The foils are piled into this slot. Finally, they are clamped using a second tantalum block which is fixed to the mount with glue. To obtain a thickness of 0.3 mm of the entire filter, both sides of the filter are mechanically milled and polished. This filter is placed in front of a thin, x-cut $LiNbO_3$ crystal (thickness 0.2 mm) to ensure that the ions are not implanted. The angular alignment of the filter has to be very precise: the aspect ratio of the Ta stripes is 100. We check the alignment by monitoring the ion current, measured behind the crystal by contacting the aluminum heat sink electrically. During the experiment, a current of 0.2 nA is observed. The duration of the irradiation is 8 h.

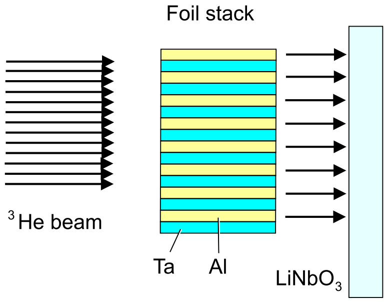

Fig. 4 Sketch of a foil stack filter (thickness 0.3 mm) to provide a grating-like ion exposure to the crystal (constrained axes, aspect ratio 1:100). The Ta stripes absorb the ions, whereas the Al stripes allow the ions to penetrate the crystal with a stop depth of 0.3 mm

After the irradiation, the crystal exhibits a rectangular spot with a modified refractive index. The magnitude of the macroscopic changes of $\Delta n_{o,e}$ is 1×10^{-4} for both light polarizations, as measured with our interferometer. This indicates that the crystal behind the filter has been subjected to ion exposure. However, no diffraction of laser light can be observed; further measurements with a light microscope and an atomic force microscope do not reveal any periodic modulation of either optical properties or the surface of the crystal. Hence, no periodic modulation of n is present. As an explanation, we assume that the ^{3}He ions are scattered inside the aluminum stripes of the filter, yielding a broadly scattered, non-parallel ion beam behind the foil stack. This would cause macroscopic material damage without distinct periodicity.

2.4.2 *Slit aperture*

In a second approach, we use a small slit made of two tantalum plates, forming a thin aperture. The setup is illustrated in Fig. 5. The tantalum plates have a size of 10×4 mm^2 and a thickness of 0.3 mm, sufficient to absorb the ^{3}He ions completely. One side plane of each plate is polished so that a small slit with a width of ≈6 μm can be constructed by bonding the plates on a tantalum carrier. The slit is mounted directly in front of the $LiNbO_3$ crystal (thickness 0.5 mm); the crystal itself is translated by a linear stage in steps of 12 μm. Hence, by moving the crystal 70 times an ion-exposure grating with a period of 12 μm is fabricated in a layer-by-layer manner; each irradiation of every single stripe lasts 8 min. We use an x-cut crystal, where the grating vector is perpendicular to the stripes and parallel to the c axis.

After the irradiation, we look for changes of the crystal color as indicator for ion exposure immediately after the irradiation. Figure 6 shows the result, obtained with a standard light microscope: we obtain a pattern with dark stripes exhibiting a lateral distance of 12 μm. For better visibility,

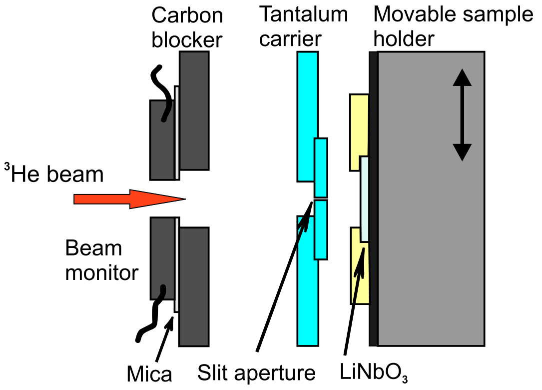

Fig. 5 Top view of the setup for grating fabrication using a slit aperture, made of two tantalum plates bonded on a tantalum carrier which is placed in front of the LiNbO$_3$ crystal. The ^{3}He ion-beam position is monitored by two carbon slabs which are mounted electrically insulated on a carbon beam block with a hole

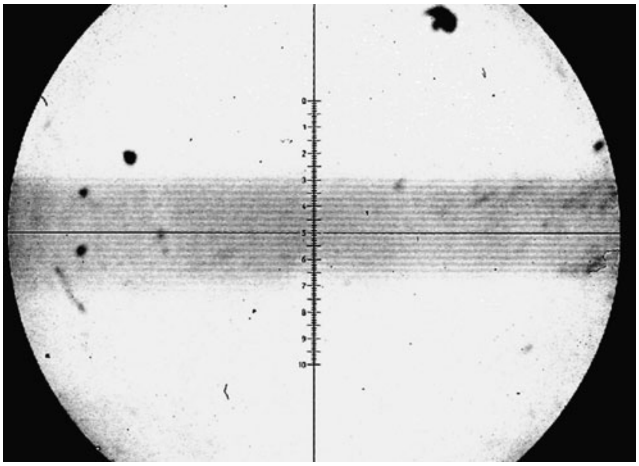

Fig. 6 Light microscope image of a successively moved LiNbO$_3$ crystal which has been stepwise irradiated through a slit aperture with a slit width of ≈6 µm. For better visibility, the contrast has been raised. Small dark stripes with a lateral distance of 12 µm are observed

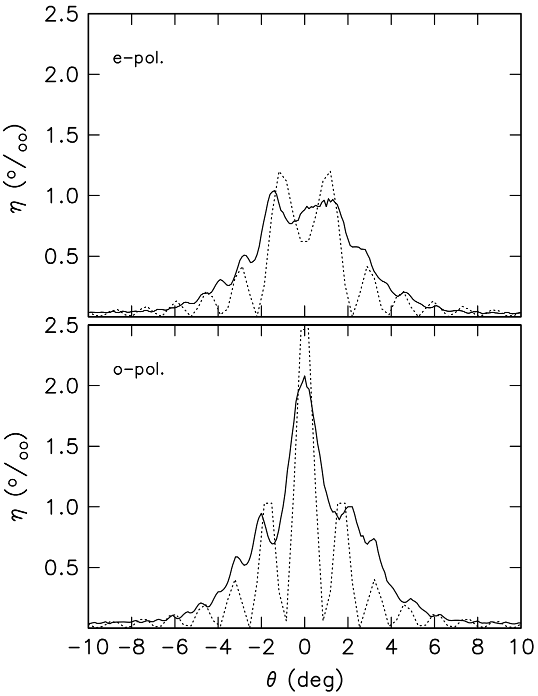

Fig. 7 Diffraction efficiency $\eta_{\mathrm{o,e}}$ vs readout beam angle θ for extraordinarily (*upper part*) and ordinarily (*lower part*) polarized probe light. The *solid lines* show experimental results, and the *dotted lines* represent fits to the data assuming a sinusoidal thick refractive-index grating according to Kogelnik's coupled wave theory [42]

the contrast has been raised in Fig. 6; the strength of the color change is quite small after the irradiation and vanishes within a few weeks.

After having the color changes removed (by waiting some weeks), we check whether a refractive-index grating is present by looking for light diffraction. For this purpose, the crystal is placed into the non-expanded beam of a He–Ne laser ($\lambda = 633$ nm). The angle θ between the laser beam and the surface normal of the crystal can be varied. Behind the crystal, the transmitted light can be observed along with diffracted light; a first diffraction order and a second order can be seen. The diffracted light intensity $I_{\mathrm{diff}}^{\mathrm{o,e}}$ of the first order is measured depending on the angle θ for ordinary and extraordinary light polarizations; the diffraction efficiency η is calculated using the formula $\eta_{\mathrm{o,e}} = I_{\mathrm{diff}}^{\mathrm{o,e}}/I_{\mathrm{trans}}$, with I_{trans} as the intensity of the transmitted light. The result is presented in Fig. 7. The measured data are shown as solid lines. Some interesting results have to be summarized. (1) A clear dependence of the diffraction efficiency on the incident light-beam angle is observed. Hence, for most effective diffraction, the Bragg condition must be fulfilled. In the figure, the zero angle is given as the deviation of the Bragg angle. (2) The shape of the curve for the diffraction efficiency of extraordinarily polarized light η_{e} yields a very strong refractive-index modulation because η shows a minimum at $\theta = 0$. (3) The diffraction efficiency of the second diffraction order is two orders of magnitude smaller compared to the first order.

Due to the presence of a Bragg condition, we can assume a thick refractive-index grating. In a first approximation, we presume a sinusoidally shaped grating and apply Kogelnik's coupled wave theory [42] to the data, yielding values for $\Delta n_{\mathrm{o,e}}$ along with a multiplication factor. This factor considers the fact that the entire size of the grating is much smaller than the diameter of the readout light beam. We find quite reasonable numbers of $\Delta n_{\mathrm{e}} = 1 \times 10^{-3}$ and $\Delta n_{\mathrm{o}} = 0.9 \times 10^{-3}$. The fits are plotted in Fig. 7 as dotted lines. The shape of the curve of the experimental data is reproduced, in particular the positions of maxima and minima. Hence, the fabrication of refractive-index gratings with ion exposure is possible and offers interesting perspectives: of course, the quality of the gratings should be improved, and their properties can be compared to those of competing techniques, such as photorefractive thermal fixing [15, 16].

2.4.3 *Microbeam irradiation*

A consequent advancement of the slit setup is the preparation of a slit-free beam spot on the target. First steps towards the realization of this concept will be presented here: a narrow ion beam (called a microbeam) is prepared for irradiations at the target station 2A using the beam-preparation system of the Bonn isochronous cyclotron [43], different to the standard irradiations which provide a simple parallel ion beam. Here the size of the beam spot can be adjusted using the last four quadrupole magnets in front of the crystal, forming an imaging system with a long object distance (≈7 m) and a short image distance (≈0.5 m). The beam emittance is controlled using the emittance-defining slits at the entrance of the beam-propagation system. A small emittance of about 1 mm mrad is needed in order to achieve a horizontal beam-spot width of less than 10 µm. In addition, the relative momentum spread must be low (about 10^{-4}) in order to keep chromatic aberrations sufficiently low. This can be achieved with the momentum-defining slit in the middle of the double monochromator system within the beamline [44].

In a first test, the horizontal width of the last analyzing slit (SX1C) has been adjusted by remote control to be 100 µm. The ion optics has been calculated using the PSI graphic TRANSPORT program [45], delivering the magnetic fields necessary within the quadrupoles. The kinetic energy of the ^{3}He beam has been assumed to be 40 MeV. For the test, a point-to-point imaging between the analyzing slit and the crystal has been adjusted with horizontal and vertical magnifications of –0.08 and –0.7, respectively. Thus, we expect a horizontal beam width of about 8 µm at the crystal. The vertical beam width has been chosen to be about 1 mm. It can be adjusted independently of the horizontal width.

The proper adjustment of the beam parameters can be checked by moving a beam viewer (fluorescent screen) into the beam. The final optimization of the slit-like beam spot is done by measuring the horizontal beam profile with a thin carbon wire. We utilize a beam-profile scanner device, consisting of a horizontally driven sliding carriage equipped with a thin carbon wire. The diameter of this wire is 50 µm. The wire is electrically connected to a sensitive pico-amperemeter (Keithley 6485, read out by a digital oscilloscope), insulated from the carrier. Thus, the current of the secondary electrons I_F induced by the ions can be measured. Hence, a spatially resolved beam profile is obtained in one dimension when the carrier is moved across the ion beam. The carbon wire is adjusted by a theodolite to be exactly parallel to the slit.

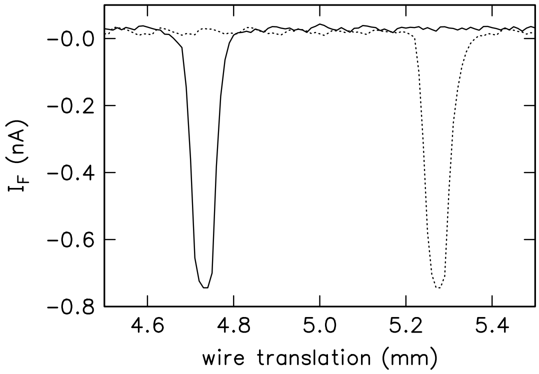

Fig. 8 Secondary electron current I_F vs lateral position of the carrier picked up with the probe wire for forward movement (*solid line*) as well as backward movement of the carrier (*dotted line*). A slightly asymmetric profile with comparable shape (if the inversion by the reversed movement within the two measurements is taken into account) is obtained, exhibiting a FWHM of 45 µm

Our experiments show that the described setup allows the successful optimization of the beamline parameters using the beam-profile scanner. After optimization, the result of the measurement of the ion beam is plotted in Fig. 8. The current I_F is plotted vs the lateral position of the carrier for a forward movement of the carrier (solid line) as well as a backward movement of the carrier (dotted line). We obtain a sharp maximum with a FWHM of 45 µm in both curves. This result remains constant even if the width of the slit is modified within the range 0.1–0.4 mm. The shape of the curve is slightly asymmetric, and those asymmetries are present in both curves in an inverted manner, as the direction of the carrier movement changes. The lateral position of the ion-beam waist at the position of the image is found to be very stable, as confirmed by repeating the experiment several times during one beamtime.

The smallest value derived for the ion-beam waist of 45 µm is slightly smaller than the diameter of the carbon probe wire. We can state that the targeted imaging scale has been successfully achieved, because the beam size does not exceed 45 µm if the slit is opened to 0.4 mm. We conclude that our ion beam is smaller than 45 µm at smaller slits; however, this has to be proven by using thinner probe wires. Due to the high lateral stability of the beam-waist position, a successful implementation of gratings in a crystal (by consecutively irradiating and moving the sample) seems promising; the experiments are currently being conducted. As a further improvement, smaller slits with a width below 0.1 mm can be used. Beyond this, the imaging technique offers another fascinating alternative: utilizing a grating instead of the slit in the object plane would provide a directly written grating in the crystal. This grating however cannot be composed from Ta and Al foils (as described above), because the energy distribution of the ions would not be sufficient after transmitting through the Al layer. It has to consist of free spanned Ta foils, which seems feasible due to the 10 times larger dimensions. Ions may be scattered at this grating, but different from the scattering problem pointed out above regarding the foil stack experiment, in this case scattered ions would not hamper the usage of a foil grating, because they would be eliminated by the ion optics behind the foils.

2.5 Channeling

The question of whether the channeling effect contributes to the results of ion exposure of $LiNbO_3$ crystals is of certain interest: if channeling occurs, the interaction of the ions with the crystal lattice is different from the case of non-channeling. Notably, channeling might be useful to avoid scattering of the ions along their trajectory in the material, yielding an improvement of the spatial resolution and hence the possibility of smaller structures. On the other hand, if channeling is present, the resulting modifications of material parameters are different; hence, we want to control the occurrence of channeling. To check whether channeling is at play in our experiments, we placed a crystal onto a double-tilt rotation stage, allowing us to change the crystal orientation angle with respect to the ion beam within the interval $\pm 0.15°$ in steps of $0.01°$. The orientation of the crystal cut is specified to be better than $\pm 0.2°$. Two semiconductor detectors are mounted at a scattering angle of 135°, allowing us to measure Rutherford back-scattered ^{3}He ions. The quantitative measurement of back-scattered ions yields no dependence on the tilt angles; however, in the case of channeling many fewer ions would be scattered into the detectors. Hence, we can rule out the appearance of channeling at the high ion energy used in our experiments. Consequently and unfortunately, channeling is not applicable as a technique to improve the spatial resolution in the modification of materials by ion exposure.

3 Ferroelectric domain reversal

Another important field of application is light conversion: $LiNbO_3$ crystals can be used for efficient second-harmonic generation (SHG). To avoid critical phase matching, quasi-phase matching is utilized: the ferroelectric axis is inverted periodically, forming periodically poled $LiNbO_3$ (so-called PPLN), and the periodic phase switching of frequency-converted light yields very effective light conversion [46, 47]. Besides simple SHG, PPLN is used to form optical parametric oscillators (OPOs), which can be taken to provide THz radiation [48, 49]. For the utilization of $LiNbO_3$ as light converters, undoped, congruently melting crystals are disadvantageous: the light beam transmitted through the material causes redistribution of charge carriers due to the photorefractive effect, resulting in a very efficient distortion of the light-intensity profile. In this context, the 'photorefractive effect' is renamed 'optical damage', which has to be avoided. Doping $LiNbO_3$ with large amounts of magnesium solves the problem: if more than 5 mol% Mg is added, the crystals are resistant against optical damage. On the other hand, the fabrication of periodically poled material becomes difficult: while undoped crystals can be poled by applying external electric fields with small finger electrodes provided by lithography methods, these techniques do not work properly with $LiNbO_3$:Mg. Hence, methods improving the ferroelectric poling feasibility of $LiNbO_3$:Mg are highly desired. One approach is the application of ultraviolet light, assisting small-sized domains to grow [50, 51]. As an alternative, the impact of ion exposure is investigated: the ions are supposed to create many defects inside the crystal which can stabilize the domain walls. We focus on two questions: firstly, the impact of ion irradiation on the coercive field E_C, defined as the external applied electric field necessary to reverse the polar axis, is investigated. Secondly, small-sized periodically poled domains are created in ion-treated $LiNbO_3$:Mg using electrode-based electric field poling.

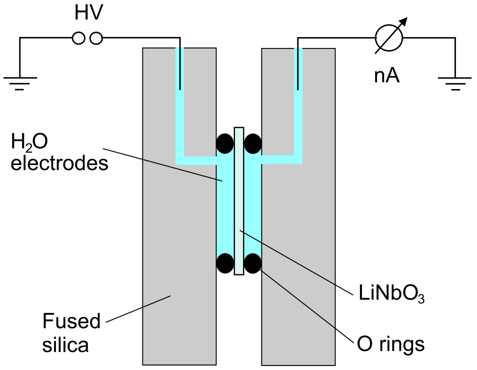

Fig. 9 Setup for applying large electric fields to the crystals: the z-cut sample is clamped between two fused silica plates using two silicone O rings, where the xy faces are contacted with liquid electrodes made of water. External fields can be applied, and the resulting currents through the crystal are monitored [32, 52]

3.1 Domain reversal and coercive field

For all experiments where the application of external electric fields is involved, we use a setup depicted in Fig. 9 [52]. The z-cut $LiNbO_3$ crystal is clamped between two fused silica plates using silicone O rings. The xy surfaces are contacted using liquid electrodes of water. External voltages are applied, and the resulting electrical current through the crystal is monitored. The two O rings cover irradiated crystal areas as well as non-treated material, as sketched in Fig. 10.

For the reversal of ferroelectric domains in $LiNbO_3$:Mg, electric fields larger than 6 kV/mm have to be applied, requiring voltages larger than 3 kV. For determination of the coercive field E_C, the voltage is increased in a ramp-like manner with a speed of 5 V/s. The field causes domains to flip, yielding compensating displacement currents which are

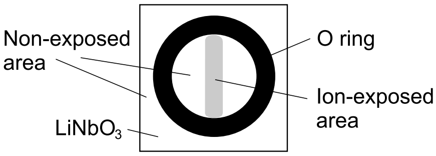

Fig. 10 Front view of the crystal clamped by the two O rings: the irradiated spot as well as non-treated material are contacted simultaneously by the liquid electrodes within the O rings [32]

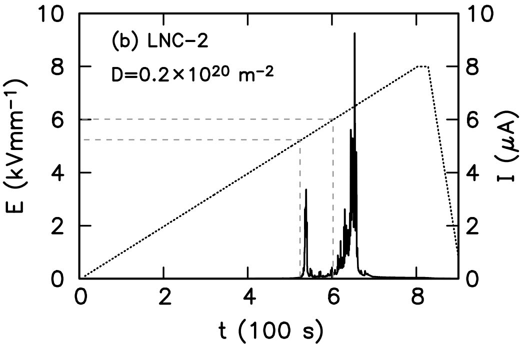

Fig. 11 Domain-reversal curve of partly irradiated $LiNbO_3$:Mg: applied external electric field (*dotted curve*) and resulting displacement current (*solid line*) vs time for a domain-reversal experiment [32]. The *dashed lines* indicate the coercive field E_C for ion-exposed and untreated material, respectively

measured by an electrometer. The coercive field E_C is defined as that value of the externally applied field at which a displacement current of 0.2 μA is exceeded [50].

Figure 11 shows the result of a domain-reversal procedure. As the voltage increases, two clearly separated peaks appear in the displacement current: the first one is caused by domain reversal within the previously irradiated spot, whereas the second peak corresponds to domain reversal of non-exposed material. This can be revealed by additional visualization of the birefringence of the crystals [32, 53]. Determining the coercive field E_C of the non-exposed material, we obtain a value of 6 kV/mm, which agrees with previous experiments [53]. The irradiated spot yields a distinctly reduced E_C of 5.4 kV/mm (see Fig. 11, dashed lines). This effect is already present at rather low ion fluences of 1×10^{19} ions/m^2. Increasing the fluence, the separation between the two peaks begins to smear out; the domain reversal still starts at a reduced E_C, but displacement currents continue to flow until the entire crystal is reversed [32]. The impact of ion treatments on E_C can be erased by annealing: after heating the crystals to 150°C for 30 min, only one peak remains. However, the E_C determined after annealing is slightly smaller than that of untreated material. By applying stronger annealing, E_C is forced back to the initial value of 6 kV/mm.

Striking similarities to the impact of UV illumination during domain reversal are obvious: ion exposure seems to cause processes in a similar manner like UV light, i.e. reducing the coercive field. This implies that the effects causing the changes in E_C are mostly caused by modifications of the electronic band structure of the crystals and not by the displacement of atoms, which is different to the modifications yielding Δn.

3.2 Periodic domain reversal

A $LiNbO_3$:Mg crystal sample of thickness 0.5 mm is subjected to ion exposure as described above. Here the beam-shaping slit in front of the crystal has the dimension 2×8 mm^2; a total ion current of 60 nA yields an ion current density of 1.7×10^{16} ions/m^2 s. The irradiation lasts 70 min; hence, the total ion fluence is 7×10^{19} ions/m^2 [54]. After the irradiation, the crystals are coated with a grating-like structured photoresist pattern (AZ1512) on the $+z$ surface. The period length of the pattern is 5.3 μm with a duty cycle of 1:4.3. For domain reversal, the crystal is subjected to high-voltage pulses of up to 5 kV and a pulse duration of 0.6 s, using the setup sketched above. After the poling procedure, the crystals are etched in HF acid, converting domain patterns into a topographical profile. This relief can be visualized by visible-light microscopy.

The result of a poling experiment is shown in Fig. 12. The mask covered the entire crystal surface shown in Fig. 12a; however, only the center part of the crystal has been penetrated by ions before. Figure 12b shows a larger magnification of the area indicated in Fig. 12a. Two results are important: firstly, in the irradiated region small-sized domains showing the periodicity of the former mask are present, whereas secondly in the non-irradiated part the typical six-fold domains [55] exhibiting much larger sizes than 5.3 μm can be found. This result clearly shows that ion exposure enables easier domain reversal compared to untreated $LiNbO_3$:Mg crystals, allowing the formation of smaller sizes of the domains in periodically poled crystals. Compared to UV supported domain engineering [56–58], the ion-exposure technique has advantages: here the irradiation process and the poling process are separated; thus, standard facilities can be used for the poling. UV light has to be present simultaneously with the electric field, requiring clever poling facilities. Of course, these experiments are not more than a proof-of principle so far; the quality of the domains can be improved by more sophisticated domain engineering. On the other hand, similarities between UV illumination and radiation damage are not surprising: both treatments yield reductions of the coercive field E_C, as shown above.

4 Electrical conductivity

The electrical DC conductivity σ can be measured with the setup shown in Fig. 9. Here the voltage will be applied in

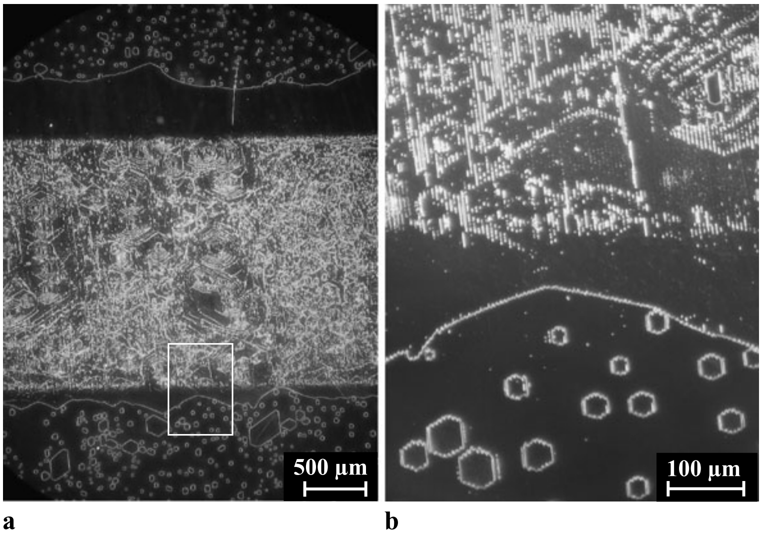

Fig. 12 Optical microscope images: (**a**) HF-etched LiNbO$_3$:Mg sample after domain reversal using a 5.3-µm mask; (**b**) region marked in (**a**) shown at higher magnification. In the irradiated sections small domains exhibiting the periodicity of the mask are present ((**b**), *upper part*), whereas in the non-exposed sections the domains are generally larger ((**b**), *lower part*) [54]

the domain-stabilizing direction: thus, we do not measure displacement currents, but can determine the conductivity of LiNbO$_3$:Mg in a straightforward way [38]. The applied voltage U is increased in steps of 0.5 kV, and the current I is monitored. After each voltage increase, we wait until a stable value of I is present. As a first result, we find that up to 2 kV the current increases superlinearly in U; for voltages from 2.5 to 4.5 kV, a linear dependence of I on U is found. From this linearity, the conductivity σ is determined. We summarize the results as follows [38]: (1) we observe both a dark conductivity σ_d as well as photoconductivity σ_{ph}. At a light intensity of $\approx$1 W/m^2 (white laboratory light), we obtain $\sigma = \sigma_d + \sigma_{ph} = 47$ pA/V m; in the dark, we get $\sigma_d = 26$ pA/V m. (2) With increasing ion fluence, the conductivity grows: the values for σ range from 2 pA/V m at 2×10^{19} ions/m^2 up to 45 pA/V m at 1.3×10^{20} ions/m^2. Without ion exposure the conductivity is much smaller than 1 pA/V m. (3) The effect of increased σ is not stable in the long term. It decreases within several days: 20 days after irradiation, we measure 50 pA/V m, going down to 30 pA/V m after 60 days. Annealing boosts the decay: after 150 min at 200°C, the conductivity has vanished. (5) Finally, we check the dependence on the irradiation orientation ($\rightrightarrows$ and $\rightleftarrows$). The result is shown in Fig. 13: the conductivity σ is plotted depending on increasing ion fluence for both configurations. We observe a strong increase of σ in $\rightrightarrows$ configuration and a much smaller growth when $\rightleftarrows$ exposure is performed. In particular, the values for σ are always much larger in the case of $\rightrightarrows$ treatments compared to $\rightleftarrows$.

Tailoring the electrical conductivity may be interesting for certain applications. In particular, it should be checked if the storage of holograms [59] is possible: the photoconductivity is large compared to the performance of classical photorefractive LiNbO$_3$ crystals doped with iron or copper [60–62]. Fast response times may be possible. On the other hand, the changes do not show long-term stability, which is a drawback for storage applications. However, this may also be an advantage: if electrical material properties similar to those of non-ion-irradiated crystals are desired, moderate annealing can remove the enhanced conductivity, without affecting refractive-index changes. They are much more long-term and thermally stable [36]. Obviously, the changes in the electrical properties are linked to changes in the electronic band structure, similar to the modifications of the coercive field as well as the color changes.

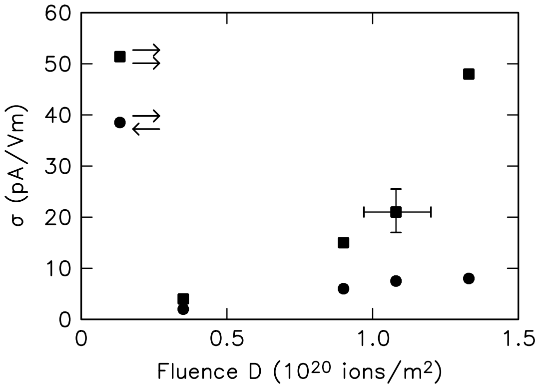

Fig. 13 Electrical conductivity σ depending on the ion fluence D and the ion irradiation orientation either parallel ($\rightrightarrows$, *squares*) or antiparallel ($\rightleftarrows$, *circles*) to the crystallographic c axis [38]

The asymmetry dependence on the irradiation configuration (Fig. 13) is striking; a similar effect has been observed regarding the refractive-index changes (Fig. 3). It can be explained taking a closer look at the crystal structure [38, 55]. The material is composed from layers of oxygen, with Li and Nb atoms located between these layers. However, the Li and Nb atoms are displaced from their symmetrical positions, forming the polar c axis of the crystals. As a consequence, the distance of a Nb atom to the next positively charged Li atom is larger in the direction along the *c* axis (3.92 angstrom) compared to the distance against the *c* axis (3.01 angstrom). Hence, the displacement energies for Nb atoms are different, depending on the direction from which a possible projectile is approaching [63].

5 Microscopic view: transmission electron microscopy

To gain insight into the microscopic processes caused by the ion exposure, transmission electron microscopy investigations (Philips model CM300UT FEG TEM/STEM operated at 300 kV) are carried out an irradiated material. Thin samples are prepared using standard techniques (cutting, grinding, dimpling, and Ar sputtering). After the dimpling, the samples are irradiated. In order to enhance the interaction between the ions and the crystal (thickness ≈40 μm after the mechanical preparation), the ions are passed through an aluminum foil (thickness 0.6 mm) placed in front of the sample, diminishing the energy of the ^3He ions to ≈20 MeV. SRIM calculations yield a transmission of 99.995% of the ions through the crystal; thus, ion implantation can be neglected. A part of the target is shielded in order to provide non-exposed material for comparison purposes. After the irradiation, the samples are finally thinned to ≈20 nm by Ar sputtering [64]. A TEM image of the sample is presented in Fig. 14. The high-resolution image shows lattice fringes of the type $\{01\bar{1}2\}$, along with characteristic circularly shaped features with diameters of 3–5 nm. These features are not observed in the non-irradiated crystal part, as shown in Fig. 14 in the inset. The contrast behavior of these features is investigated in more detail using TEM bright-field imaging mode in out-of-focus conditions [65]. In under-focus condition, the circles give rise to dark contrast in the center, surrounded by a bright circular fringe. This contrast behavior due to differences in the inner potential is explicable under the assumption of an increased material density within the circular features with respect to the surrounding material [64].

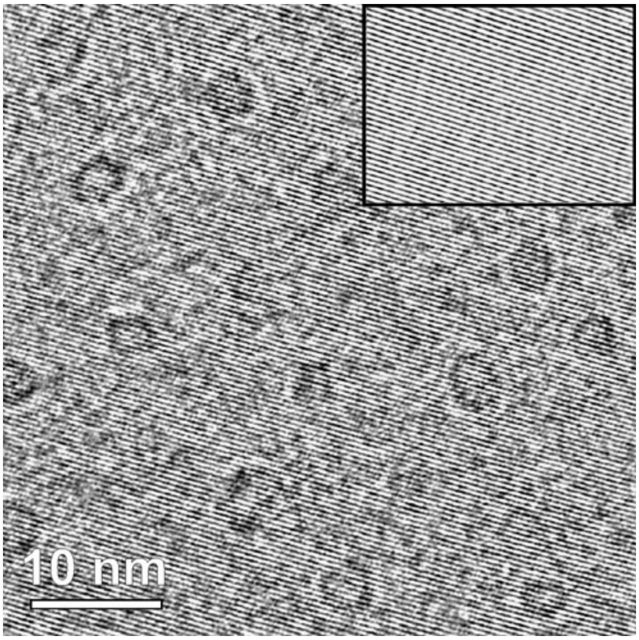

Fig. 14 TEM lattice fringe image of ^3He-irradiated $LiNbO_3$ exhibiting circular damage features. The *inset* shows a non-treated crystal region for comparison: no circular features are present [64]

The presence of circularly shaped material of increased density is compatible with the assumption of continuous amorphous tracks as a consequence of thermal spikes. In order to create these amorphous tracks by an electronic interaction of a projectile with the target material, stopping powers in the range of 1–5 keV/nm are required [66–69]. An ion exhibiting a sufficiently large stopping power is capable of dissipating enough energy to melt a cylindrically shaped volume. Since a thin layer is cut from the crystal during TEM specimen preparation, a circular plate remains. The typical diameter of such amorphous tracks in insulators is known to be around 5 nm, agreeing well with the diameter of the features shown in Fig. 14 [70]. However, the stopping power must exceed a certain threshold value to be able to form those tracks. We can exclude the primary ^3He ions: the stopping power is too small. Assuming knock-on collisions of the ^3He ions with Nb atoms, it will transfer 2.4 MeV onto the Nb atom in a central collision. The energy loss of such a displaced Nb atom is 3 keV/nm and thus sufficient to form an amorphous track. The same is valid for initial ^3He knock-on processes with an O atom: an energy of 10 MeV is transferred in a central collision, and the energy loss is 2.5 keV/nm. Finally, an energy of 17 MeV can be transferred to a Li atom; however, the energy loss of Li is 0.5 keV/nm and thus too small to be responsible for amorphous track formation. Hence, it is reasonable to attribute the observed damage effects to two-step mechanisms via $^3He \rightarrow Nb$ and $^3He \rightarrow O$ knock-on collisions [64]. The amorphization leads to a loss of Li (as the most volatile atom species in the target), leaving a Li-deficient amorphous track. Considering the phase diagram of $LiNbO_3$, the compound $LiNb_3O_8$, exhibiting larger density but similar refractive index [71], is a probable candidate, fitting well to the observed contrast behavior in the TEM bright-field images. Furthermore, the assumption of the presence of a Li-deficient phase is also supported by X-ray absorption spectroscopy experiments [72].

6 Mechanism of radiation damage in lithium niobate crystals

The TEM results imply a two-step mechanism responsible for the material modifications: the high-energy ^3He ions do not directly cause strong effects in the crystals, but initiate knock-on processes with target atoms, and those displaced atoms have enough energy loss $\Delta E/\Delta x$ yielding thermal spikes. This model explains several experimental observations. Assuming such two-step processes, it becomes clear that the refractive-index changes $\Delta n_{\mathrm{o,e}}(d)$ are correlated with the density of vacancies c_{vac} (Sect. 2.2.1). Furthermore, it is intuitively clear that irradiation with swift heavy ions is more effective compared to that using low-mass ions: they already exhibit energy losses large enough to form thermal spikes. Hence, in the case of swift heavy ions a connection of the material changes with the energy loss function $\Delta E/\Delta x$ is reasonable, whereas in the case of low-mass, high-energy ions the two-step process is required. The asymmetry occurring upon changing the direction of the c axis with respect to the ion beam is another strong argument supporting the model of two-step processes: it is clear that different displacement energies of Nb (and Li ions as indirectly involved ion) directly influence the energy transmission from ^{3}He ions onto the Nb ions during the knock-on collision. Thus, the efficiency of the knock-on processes is depending on the direction of the ion irradiation.

The presence of amorphous channels in the crystals is not directly causing the macroscopic refractive-index change. The investigations using swift heavy ions for waveguide fabrication show that accumulating large material damage finally can create an amorphous layer, exhibiting a reduced refractive index of 2.1 [73]. However, the experiments presented here yield an increase Δn_{e} of the extraordinary refractive index which would not be present if large-volume amorphization has taken place. The channels of modified, more dense material however cause long-reaching stress changes inside the crystals. This yields strain of the crystal structure, affecting the refractive index via modifications of the spontaneous polarization P_{S}, as described e.g. in Ref. [74] and already discussed in context with femtosecond writing of waveguiding structures [37, 75]. However, a consistent theory able to describe all features of Δn such as the dependence on the ion fluence and accounting for the obvious differences between ion-induced Δn and femtosecond laser written Δn is not available today. Furthermore, it is reasonable that Δn is rather long-term stable: removing Δn requires large thermal activation energy to get the amorphous channels crystallized again and to relax the mechanical stress induced by the channels.

The other effects induced by ion exposure are dramatically less stable: color changes, modifications of the coercive field E_{C}, and electrical conductivity σ can be removed easily by waiting (at room temperature) or moderate annealing (e.g. 100C or 150°C for 30 min). As pointed out above, these modifications can be attributed to changes within the electronic band structure, as all these effects can also be induced by other treatments (such as UV illumination) which are not able to redistribute ions within the crystal. It is of certain interest to focus on the asymmetric behavior of the electrical conductivity: the asymmetry is quite distinct; hence, it is supposed to be caused by the secondary ions provided by the knock-on processes discussed above. The asymmetry appears due to the anisotropic displacement energy. As a consequence, a direct modification of σ by the primary ^{3}He ions can be neglected.

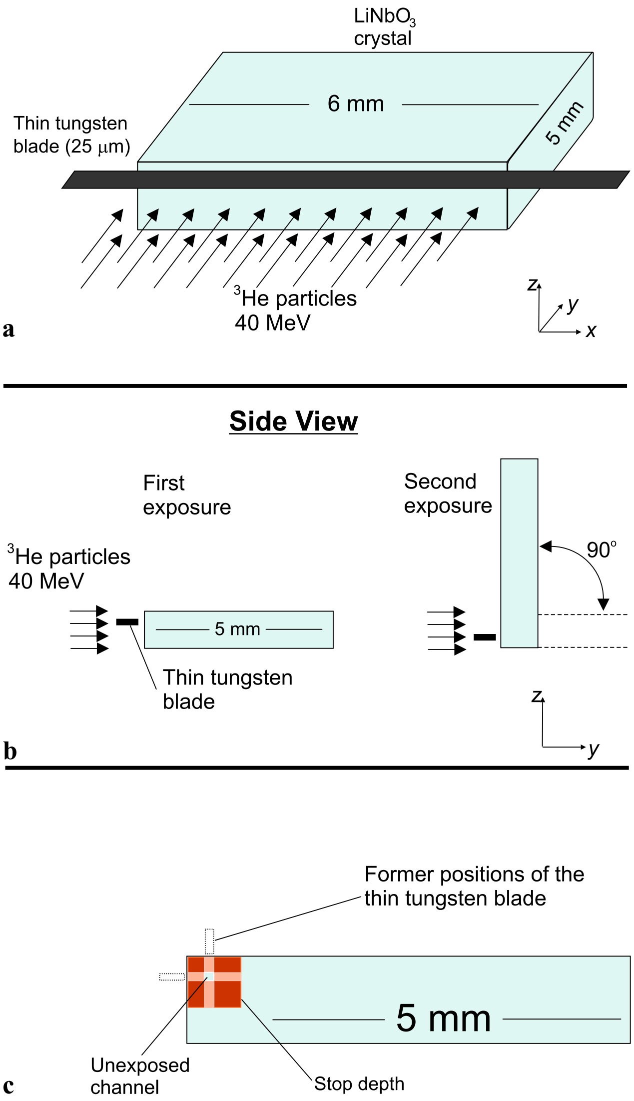

Fig. 15 Setup for the fabrication of embedded waveguides in LiNbO$_3$: (**a**) a thin tungsten blade, placed in front of the crystal surface, blocks the ions, creating a thin shadow within the ion beam. (**b**) The side view depicts two irradiation geometries used subsequently under an angle of 90°. The tungsten blade yields a non-irradiated layer. After the first exposure, the crystal is rotated. (**c**) The two ion exposures yield two ion beam shadows behind the former positions of the tungsten blade. An unexposed channel is created in the intersecting region of the two non-irradiated shadow layers [76]

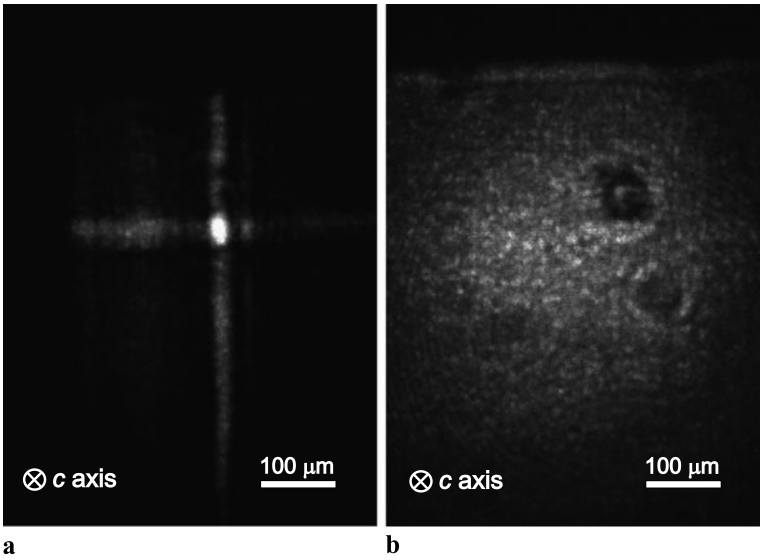

Fig. 16 Light distribution at the output surface of a 5-mm-long crystal (**a**) with light coupled into the non-irradiated channel and (**b**) with light coupled into a crystal part which has not been subjected to any ion exposure [76]

7 Application: embedded polarization-depending waveguides

The fabrication of an embedded waveguide in a $LiNbO_3$ crystal will be discussed [76]. The basic idea is as follows: irradiating a crystal diminishes the ordinary refractive index. Hence, creating a setup which provides a broadly ion-exposed crystal volume with a non-irradiated channel inside will produce a light-guiding structure, where the light is traveling through non-modified material. This material still has the optical properties of untreated $LiNbO_3$. To provide a suitable setup, we choose an arrangement shown in Fig. 15. A thin tungsten blade (thickness 25 μm, width 1 mm) is spanned directly in front of the crystal surface. The width of the blade is sufficient to absorb the ions; hence, in the ion beam, a thin shadow is created where no irradiation takes place. The crystal is subjected to a homogeneous ion beam except for this thin shadow; hence, a thin layer of untreated material is remaining. After a first irradiation, the crystal is rotated by 90°, and a second irradiation is carried out (Fig. 15b). Thus, a channel of non-exposed material is remaining, surrounded by crystal parts irradiated either once or twice (see Fig. 15c).

To check whether light-guiding structures can be prepared in this manner, a standard fiber-to-waveguide setup is used. Light of a He–Ne laser is directed onto one (input) crystal surface, and the light intensity at the opposing (output) crystal surface is imaged onto a CCD chip. The result is depicted in Fig. 16: if the light is coupled at the position of the non-exposed channel, a small, but bright, light spot is observed at the output surface. If the light is coupled into a crystal volume which has not been subjected to ion exposure, a bright light cone is measured. Hence, the light is guided inside the unexposed crystal channel, and the light intensity distribution shows that a monomode waveguide is present with a lateral size of 30 μm [76]. If the *c* axis is chosen parallel to the channel, as indicated in Fig. 16, the light guiding is independent of the light polarization at the input surface, because it is always ordinarily polarized within the crystal. When a crystal geometry with the *c* axis perpendicular to the channel is chosen, both polarizations can be addressed at the input surface. Thus, ordinarily polarized light is guided, whereas extraordinarily polarized light is deflected [76]. Hence, a polarization-sensitive embedded waveguide is provided. The losses of the waveguide however are quite large; we estimate a value of 5 dB/cm. We consider this result as a proof-of principle showing the potential of the method; current efforts are aiming at further improving the performance of the waveguide.

8 Conclusion

Irradiation of lithium niobate crystals with low-mass, high-energy ions is a powerful tool for providing tailored, structured components for modern optics. Large, stable, and structured changes of the refractive index have been obtained, and the underlying two-step mechanism based on knock-on collisions of the ions with crystal atoms has been elucidated. The irradiation assists the feasibility of the formation of small domains in Mg-doped lithium niobate crystals and creates dark- and photoconductivity. These achievements pave the road towards further optimization of integrated optical components for light sources and light processors.

Acknowledgements Technical support by the cyclotron team of the Helmholtz-Institut is gratefully acknowledged. Fruitful and enlightening discussions with B. Andreas, K. Buse, I. Breunig, T. Jungk,

M. Kösters, H. Modrow, H. Steigerwald, and T. Vitova are highly appreciated. Financial support by the Deutsche Forschungsgemeinschaft, grants FOR557-B1 and R2, is gratefully acknowledged.

References

1. H.J. Coufal, D. Psaltis, G.T. Sincerbox, *Holographic Data Storage* (Springer, Berlin, 2000)
2. R.M. Shelby, J.A. Hoffnagle, G.W. Burr, C.M. Jefferson, M.-P. Bernal, H. Coufal, R.K. Grygier, H. Guenther, R.M. Macfarlane, G.T. Sincerbox, Opt. Lett. **22**, 1509 (1997)
3. K. Peithmann, A. Wiebrock, K. Buse, Appl. Phys. B **68**, 777 (1999)
4. F.H. Mok, Opt. Lett. **18**, 915 (1993)
5. A. Ashkin, G.D. Boyd, J.M. Dziedzic, R.G. Smith, A.A. Ballman, J.J. Levinstein, K. Nassau, Appl. Phys. Lett. **9**, 72 (1966)
6. A.M. Glass, D. von der Linde, T.J. Negran, Appl. Phys. Lett. **25**, 233 (1974)
7. V. Leyva, G.A. Rakuljic, B. O'Conner, Appl. Phys. Lett. **65**, 1079 (1994)
8. S. Breer, H. Vogt, I. Nee, K. Buse, Electron. Lett. **34**, 2419 (1999)
9. R.C. Alferness, R.V. Schmidt, E.H. Turner, Appl. Opt. **18**, 4012 (1979)
10. W.K. Burns, A.B. Lee, A.F. Milton, Appl. Phys. Lett. **29**, 790 (1976)
11. V. Ramaswamy, M.D. Divino, R.D. Standley, Appl. Phys. Lett. **32**, 644 (1978)
12. R.V. Schmidt, I.P. Kaminow, Appl. Phys. Lett. **25**, 458 (1974)
13. D. Kip, Appl. Phys. B **67**, 131 (1998)
14. C. Becker, A. Greiner, T. Oesselke, A. Pape, W. Sohler, H. Suche, Opt. Lett. **23**, 1194 (1998)
15. J.J. Amodei, W. Phillips, D.L. Staebler, IEEE J. Quantum Electron. **7**, 321 (1971)
16. K. Buse, S. Breer, K. Peithmann, S. Kapphan, M. Gao, E. Krätzig, Phys. Rev. B **56**, 1225 (1997)
17. J. Hukriede, B. Gather, D. Kip, E. Krätzig, Phys. Status Solidi A **172**, R3 (1999)
18. K. Peithmann, J. Hukriede, K. Buse, E. Krätzig, Phys. Rev. B **61**, 4615 (2000)
19. G.L. Destefanis, P.D. Townsend, J.P. Galliard, Appl. Phys. Lett. **32**, 293 (1978)
20. G.L. Destefanis, J.P. Galliard, E.L. Ligeon, S. Valette, B.W. Farmery, P.D. Townsend, A. Perez, J. Appl. Phys. **50**, 7898 (1979)
21. P.J. Chandler, P.D. Townsend, Nucl. Instrum. Methods Phys. Res. B **19–20**, 921 (1987)
22. E. Glavas, L. Zhang, P.J. Chandler, P.D. Townsend, Nucl. Instrum. Methods Phys. Res. B **32**, 45 (1988)
23. L. Zhang, P.J. Chandler, P.D. Townsend, Nucl. Instrum. Methods Phys. Res. B **59–60**, 1147 (1991)
24. H. Hu, F. Chen, B.-R. Shi, K.-M. Wang, D.-Y. Shen, Appl. Opt. **40**, 3759 (2001)
25. H. Hu, F. Lu, F. Chen, B.-R. Shi, K.-M. Wang, D.-Y. Shen, J. Appl. Phys. **89**, 5224 (2001)
26. G.G. Bentini, M. Bianconi, M. Chiarini, L. Correda, C. Sada, P. Mazzoldi, N. Argiolas, M. Bazzan, R. Guzzi, J. Appl. Phys. **92**, 6477 (2002)
27. J. Olivares, G. Garcia, A. Garcia-Navarro, F. Agullo-Lopez, O. Caballero, A. Garcia-Cabanes, Appl. Phys. Lett. **86**, 183501 (2005)
28. A. Rivera, J. Olivares, G. Garcia, J.M. Cabrera, F. Agullo-Rueda, F. Agullo-Lopez, Phys. Status Solidi A **206**, 1109 (2009)
29. D.F. Nelson, R.M. Mikulyak, J. Appl. Phys. **45**, 3688 (1974)
30. B. Andreas, K. Peithmann, K. Buse, K. Maier, Appl. Phys. Lett. **84**, 3813 (2004)
31. J.F. Ziegler, J.P. Biersack, U. Littmark, *The Stopping and Range of Ions in Solids* (Pergamon, New York, 1985)
32. L. Jentjens, H. Hattermann, K. Peithmann, M. Haaks, K. Maier, M. Kösters, J. Appl. Phys. **103**, 034104 (2008)
33. K. Peithmann, M.-R. Zamani-Meymian, M. Haaks, K. Maier, B. Andreas, I. Breunig, J. Opt. Soc. Am. B **23**, 2107 (2006)
34. B. Andreas, I. Breunig, K. Buse, ChemPhysChem **6**, 1 (2005)
35. K. Peithmann, A. Wiebrock, K. Buse, E. Krätzig, J. Opt. Soc. Am. B **17**, 586 (2000)
36. M.-R. Zamani-Meymian, L. Jentjens, N.L. Raeth, K. Peithmann, K. Maier, Appl. Phys. A **98**, 909 (2010)
37. J. Burghoff, H. Hartung, S. Nolte, A. Tünnermann, Appl. Phys. A **86**, 165 (2007)
38. L. Jentjens, N.L. Raeth, K. Peithmann, K. Maier, J. Appl. Phys. **109**, 124104 (2011)
39. E.R. Hodgson, F. Agullo-Lopez, Nucl. Instrum. Methods Phys. Res. B **32**, 42 (1988)
40. R. Pareja, R. Gonzalez, M.A. Pedrosa, Phys. Status Solidi A **84**, 179 (1984)
41. F. Jermann, M. Simon, R. Böwer, E. Krätzig, O.F. Schirmer, Ferroelectrics **165**, 319 (1995)
42. H. Kogelnik, Bell Syst. Tech. J. **48**, 2909 (1969)
43. F. Hinterberger, H.G. Ehrlich, K. Euler, W. Hehemeyer, P. Meyer, P.V. Rossen, B. Schuller, G. Welp, Nucl. Instrum. Methods **130**, 335 (1975)
44. F. Hinterberger, *Physik der Teilchenbeschleuniger und Ionenoptik* (Springer, Berlin, 2008)
45. U. Rohrer, P.S.I. Note (2005). http://pc532.psi.ch/trans.htm, based on a CERN–SLAC–FERMILAB version by K.L. Brown, D.C. Carey, C. Iselin, and F. Rothacker, Software and Information, CERN Rep. 80 (1980)
46. G.A. Magel, M.M. Fejer, R.L. Byer, Appl. Phys. Lett. **56**, 234 (1989)
47. M. Yamada, N. Nada, M. Saitoh, K. Watanabe, Appl. Phys. Lett. **62**, 435 (1993)
48. R. Sowade, I. Breunig, I.C. Mayorga, J. Kiessling, C. Tulea, V. Dierolf, K. Buse, Opt. Express **17**, 22303 (2009)
49. I. Breunig, J. Kiessling, R. Sowade, B. Knabe, K. Buse, New J. Phys. **10**, 073003 (2008)
50. M.C. Wengler, B. Fassbender, E. Soergel, K. Buse, J. Appl. Phys. **96**, 2816 (2004)
51. C.E. Valdivia, C.L. Sones, S. Mailis, J.D. Mills, R.W. Eason, Ferroelectrics **340**, 75 (2006)
52. M.C. Wengler, M. Müller, E. Soergel, K. Buse, Appl. Phys. B **76**, 393 (2003)
53. M.C. Wengler, U. Heinemeyer, E. Soergel, K. Buse, J. Appl. Phys. **98**, 064104 (2005)
54. L. Jentjens, K. Peithmann, K. Maier, H. Steigerwald, T. Jungk, Appl. Phys. B **95**, 441 (2009)
55. R.S. Weis, T.K. Gaylord, Appl. Phys. A **37**, 191 (1985)
56. H. Steigerwald, F. Luedke, K. Buse, Appl. Phys. Lett. **94**, 032906 (2009)
57. A.C. Muir, C.L. Sones, S. Mailis, R.W. Eason, T. Jungk, Á. Hoffmann, E. Soergel, Opt. Express **16**, 2336 (2008)
58. C.L. Sones, A.C. Muir, Y.J. Ying, S. Mailis, R.W. Eason, T. Jungk, Á. Hoffmann, E. Soergel, Appl. Phys. Lett. **92**, 072905 (2008)
59. D. Gabor, Nature **161**, 777 (1948)
60. E. Krätzig, H. Kurz, Ferroelectrics **13**, 295 (1976)
61. E. Krätzig, Ferroelectrics **21**, 635 (1978)
62. E. Krätzig, R. Orlowski, Ferroelectrics **27**, 241 (1980)
63. D. Kaletta, K. Ehrlich, J. Nucl. Mater. **51**, 227 (1974)
64. M.-R. Zamani-Meymian, K. Peithmann, K. Maier, H. Schmid, W. Mader, J. Phys., Condens. Matter **21**, 075402 (2009)
65. H.K. Schmid, J. Microsc. **194**, 192 (1999)
66. B. Canut, R. Brenier, A. Meftah, P. Moretti, S.O. Salem, S. Ramos, P. Thevenard, M. Toulemonde, Nucl. Instrum. Methods Phys. Res. B **91**, 312 (1994)
67. N. Itoh, A.M. Stoneham, Nucl. Instrum. Methods Phys. Res. B **146**, 362 (1998)

68. A. Meftah, F. Brisard, J.M. Costantini, M. Hage-Ali, J.P. Stoquert, F. Studer, M. Toulemonde, Phys. Rev. B **48**, 920 (1993)
69. G. Szenes, Nucl. Instrum. Methods Phys. Res. B **191**, 54 (2002)
70. M. Toulemonde, C. Dufour, A. Meftah, E. Paumier, Nucl. Instrum. Methods Phys. Res. B **166–167**, 903 (2000)
71. L.O. Svaasand, M. Eriksrud, A.P. Grande, F. Mo, J. Cryst. Growth **18**, 179 (1973)
72. T. Vitova, M.-R. Zamani-Meymian, K. Peithmann, K. Maier, J. Hormes, J. Phys., Condens. Matter **21**, 495401 (2009)
73. A. Garcia-Navarro, F. Agullo-Lopez, J. Olivares, J. Lamela, F. Jaque, J. Appl. Phys. **103**, 093540 (2008)
74. Y. Jiang, K.-M. Wang, X.-L. Wang, F. Chen, C.-L. Jia, L. Wang, Y. Jiao, F. Lu, Phys. Rev. B **75**, 195101 (2007)
75. J. Burghoff, S. Nolte, A. Tünnermann, Appl. Phys. A **89**, 127 (2007)
76. K. Peithmann, M.-R. Zamani-Meymian, M. Haaks, K. Maier, B. Andreas, K. Buse, H. Modrow, Appl. Phys. B **82**, 419 (2006)